Construction and Building Materials 419 (2024) 135408

Contents lists available at ScienceDirect

Construction and Building Materials

journal homepage: www.elsevier.com/locate/conbuildmat

Lap splice assessment of GFRP rebars in reinforced concrete beams under flexure

Jesús D. Ortiz [a,*], Zahid Hussain [a], Seyed-Arman Hosseini [b], Brahim Benmokrane [b], Antonio Nanni [a]

[a] Department of Civil and Architectural Engineering, University of Miami, Coral Gables, FL 33146, USA
[b] Department of Civil Engineering, University of Sherbrooke, QC J1K 2R1, Canada

ARTICLE INFO

Keywords:
Bond failure
Bond stresses
Lap-Splice length
GFRP rebars
Rebar slippage

ABSTRACT

To increase the knowledge and experience gained from the existing literature regarding the bond behavior of glass fiber-reinforced polymer (GFRP) rebars, a total of sixteen full-scale GFRP-reinforced concrete beams were subjected to a four-point bending test. The GFRP reinforcement comprised a single M16 (No.5) GFRP sand-coated bar without confinement reinforcement in the constant moment region. The research parameters encompassed three different lap-spliced lengths (i.e., 40-, 60- and 80-d_b) and two distinct concrete clear covers (i.e., 19 mm and 38 mm) to assess their impact on bond strength and failure modes. Strain gauges along the GFRP rebar and small potentiometers positioned at the end of the splice within the constant moment zone allowed detailed measurements. Rebar slippage in lap-spliced specimens was observed to have a limited impact on bond stress transfer capacity and member flexural stiffness until reaching maximum slippage. Concrete cover significantly influenced the behavior of lap-spliced GFRP-RC beams, with 38 mm-cc specimens exhibiting an average 21% higher capacity compared to 19 mm-cc specimens. The ACI expression exhibited an average overestimation of 24% for 19 mm-cc specimens, whereas for 38 mm-cc specimens, it offered a more accurate estimation, with only a 10% over-prediction. However, the computed lap splice length to achieve the required tensile stress was reduced from the one required by ACI due to extra factors implemented in the development length equation. This aligns with prior research findings that identified unconservative values of bond stress when employing the ACI provisions for specific combinations of parameters, highlighting the necessity for refinements in predictive models.

1. Introduction

The use of non-metallic reinforcement, such as fiber-reinforced polymer (FRP) reinforcing bars, has emerged as a viable alternative for addressing corrosion problems in steel-reinforced concrete (RC) structures. A significant increase in the utilization of FRP bars has been observed in recent decades, particularly in regions with corrosion concerns [1–5]. Among the available types (i.e., glass, carbon, aramid, and basalt), Glass-FRP (GFRP) bars have gained considerable attention due to their cost advantage over Carbon-FRP bars [6]. The improvement of material properties (i.e., the second generation of GFRP bars with a modulus of elasticity of minimum 60 GPa (8700 ksi)), the introduction of new standards (i.e., the new ACI 440.11–22 code [7] and ASTM D8505–23 [8]), and the adoption of innovative construction techniques have enabled the utilization of the full potential of GFRP rebars in concrete structures. Nevertheless, certain limitations delay their complete integration as a reinforcement material. Existing development length equations yield large values, leading to challenges in detailing and congestion of bars, particularly at exterior supports [9,10]. Additionally, lap splicing is the commonly used method is construction for transferring forces from on rebar to another. However, due to the brittle nature of GFRP bars, they cannot be bent and are therefore produced in smaller lengths compared to steel bars. Consequently, lap splices are more frequently required for GFRP bars [11].

The equation specified in ACI 440.11 building code [7] was derived by Wambeke and Shield [12] using a procedure similar to that employed for steel reinforcement in ACI 318 [13,14]. However, due to a lack of comprehensive data on embedment or lap splice length, conservative assumptions were made, and the influence of certain parameters was disregarded. Since the initial inclusion of the equation in the guidelines,

---

[*] Corresponding author.
E-mail address: jesus.ortiz@miami.edu (J.D. Ortiz).

https://doi.org/10.1016/j.conbuildmat.2024.135408
Received 15 September 2023; Received in revised form 6 January 2024; Accepted 8 February 2024

numerous research projects have been dedicated to assessing and refining its accuracy.

Several research studies have been conducted to understand the crucial role of bond behavior between reinforcement and concrete in structural performance. In the context of conventional steel-reinforced structure, achieving an adequate development length is essential for steel reinforcement to reach its yield strength, thereby allowing concrete members to achieve their ultimate strength without compromising composite action [15]. Concerning GFRP bars, a proper development length is vital to prevent bond failures and ensure stress transfer from reinforcement to concrete without excessive slip [16]. However, in GFRP-reinforced concrete beams, characterized by the elastic-up-to-failure behavior of the FRP rebar, there is no specific tensile strength value that the rebar must reach before bond failure. The elements are commonly designed as either under- or over-reinforced sections, potentially constraining the maximum tensile stress faced by the rebar. Furthermore, bond characteristics play a key role in enabling their application in concrete structures [6,17]. Surface treatments can be broadly categorized into four types: sand-coated, indented/grooved, ribbed, and helically wrapped, with potential combinations among them. Each one with unique characteristics. There still is not standardization for surface characteristics, unlike steel bars [18].

The bond of reinforcing bars to concrete comprises various components, including chemical adhesion, frictional resistance, and mechanical interlock due to surface irregularities [19]. Interfacial bond stresses facilitate the transfer of tension forces to reinforcing bars within concrete, ensuring their proper function in reinforced concrete structures [20–22]. The bond behavior of FRP rebars shares similarities with conventional steel bars, although it is influenced by a larger number of parameters [17,21]. Embedment or lap splice length [6,18,21,23–25], bar diameter [18,22,24], concrete cover [6,24], concrete compressive strength [6,20,21,23,24,26], placement of the reinforcement [18,23], bar spacing [10,27], confinement reinforcement [6,10,24,27,28], fiber type [29], modulus of elasticity of the GFRP bar [23], surface treatment [18,22,26,30], among others, have been suggested as influential parameters in the bond strength of flexural RC elements. Furthermore, the influence of extra parameters like harsh environmental conditions has also been studied [26]. Various test setups have been utilized to study the bond behavior of GFRP rebars, such as pull-out tests, hinged beam tests, notched beam tests, inverted half-beam tests, half-beam tests and splice beam tests with three- or four-point bending. The pullout test is easy and quick but cannot accurately represent the actual stress condition in flexural members. Other tests, such as the hinged- and notched-beam tests, while representing a flexural condition, limit the cracks formation conditions typical of a flexural element. Using results from many sources without standardized methods could incorporate an additional uncertainty into the equation.

The definition of a bond stress distribution has been the focus of numerous research studies. Although it is typically accepted to assume a uniform stress distribution along the embedded or lap-spliced length. In reality, a non-uniform distribution is more likely to occur. Bond strength has been proved to decrease as the embedment length and bar diameter increase, but not in the same proportion [18]. So far, no unified model is available that can be applied to the general bond behavior of GFRP bar [6]. Makhmalbaf & Razaqpur [16] proposed the modified form of the logistic growth function as distribution function of tensile strain along the developed bar. However, specific points of strain and length are required to find the parameters of the function.

The findings from the available literature present conflicting perspectives regarding the reliability of the current equation in accurately predicting bond strengths. While some researchers argue that the equation produces overly conservative results [6,10,16,20,25,27,31], others contend that it may lead to potential overestimation of bond strength [11,23,24]. Furthermore, some authors have stated that the equation yields high accuracy predictions [6,17,21]. Several recommended bond strength models targeting different influencing parameters can be found in the literature. In 2012, Choi et al. [32] proposed an updated model similar to the one by Wambeke and Shield but included the relation between the maximum and minimum clear cover. Later, in 2013, Esfahani et al. included the effect of confinement reinforcement for the first time, introducing an extra parameter for surface treatment. Additional attempts to update or propose a development length equation have been made by researchers such as Choi et al. [33], Basaran & Kalkan [20], Al-salloum et al. [27], Wu et al. [34], and, more recently, Arman et al. [11]. However, none of these equations have been adopted by design provisions.

This paper presents the findings of an experimental study aimed at evaluating the bond stresses between the new generation of GFRP sand-coated bars and the surrounding conventional concrete. The specimens consisted of under-reinforced lap-spliced concrete beams subjected to a four-point bending test. A single M16 (No.5) rebar was utilized as the main reinforcement. Three different lap splice lengths and two different concrete covers were analyzed. The instrumentation included strain gauges along the rebar and small potentiometers positioned at the end of the splice, located within the constant moment zone. The primary objective of the study was to assess the current ACI 440.11–22 equation to enhance the knowledge and experience gained from the existing literature regarding bond behavior.

2. Experimental program

2.1. Materials properties

Full-scale RC-beam specimens were cast using standard structural ready-mix concrete, specifically designed to achieve a targeted strength of 35 MPa (5070 psi). The concrete mixture incorporated a coarse aggregate with a nominal size of 19 mm (3/4 in.). To optimize workability, the concrete slump was set at approximately 150 mm (6.0 in.). In total, four different batches were utilized for casting the full specimens. From each concrete batch, representative 100 ×200 mm (4 ×8 in.) cylinders were cast. Both the beam specimens and cylinders were demolded after one day of casting and subsequently moist cured for 7 days under controlled laboratory conditions. On the day of beam testing, the cylinders were tested according to ASTM C39 [35] to determine their compressive strength. An average compressive strength of 40.1 MPa (5830 psi) was obtained with a standard deviation of 3.1 MPa (450 psi) (coefficient of variation of 7.7%). The modulus of elasticity of the concrete was computed according to ACI 318–19 [13] based on the 28-day compressive strength: $E_c = 4700\sqrt{f'_c}$ (in SI).

The longitudinal reinforcement of the beam specimens comprised an M16 (No.5) GFRP rebar with a nominal diameter of 15.9 mm (0.625 in.) and a nominal area of 199 mm^2 (0.31 in.^{2}) as per ASTM D8505 [8] (this rebar size is a representative reinforcement size commonly used in RC-beams). The rebar was pultruded using continuous ECR (Electrical Corrosion Resistance) fibers impregnated in a thermosetting vinyl-ester resin, resulting in a mass fiber content of 83%. The surface enhancement of the rebar consisted of a thin sand coating. Pull-out tests were carried out to determine the bond strength as per ASTM D7913/D7913–20 [36]. Table 1 lists the main physical-mechanical properties of the reinforcing GFRP bar as determined by tensile tests on representative samples. M16 (No.5) GFRP bars were also utilized as bottom reinforcement up to the point of application of the load to support the cage (see Fig. 1). Similarly, GFRP M13 (No.4) stirrups were employed as transverse reinforcement throughout, with exception of the constant moment zone, to avoid potential bond enhancement through confinement effects. Steel Grade 420 (Grade 60) was used for top longitudinal reinforcement for construability purposes. The steel rebars were tested according to ASTM A706/A706M [37], where the yield strength of the reinforcing steel was found to be 480 MPa (70 ksi).

Table 1
Physical-Mechanical properties of the GFRP rebar.

Characterization	Standard	Average (μ)	Std Dev (σ)
Fiber mass content	ASTM D2584	83%	0.2%
Glass transition temperature	ASTM E1356	113 °C (235 °F)	9.6 °C (17.2 °F)
Degree of cure	CSA S807	99%	0.3%
Measured cross-sectional area	ASTM D7205	238 mm^2 (0.369 $in.^2$)	3.5 mm^2 (0.0054 $in.^2$)
Ultimate tensile force	ASTM D7205	264 kN (59.3 kip)	6 kN (1.35 kip)
Ultimate tensile strength	ASTM D7205	1326 MPa (192 ksi)	30.1 MPa (4.4 ksi)
Tensile modulus of elasticity (E_f)	ASTM D7205	64.9 GPa (9416 ksi)	1.07 GPa (154 ksi)
Ultimate tensile strain	ASTM D7205	2.04%	0.06%
Ultimate transverse shear force	ASTM D7617	90 kN (20.2 kip)	1.2 kN (0.28 kip)
Ultimate transverse shear strength	ASTM D7617	226 MPa (33 ksi)	3.1 MPa (0.4 ksi)
Moisture absorption (24 h)	ASTM D570	0.07%	0.003%
Bond strength	ASTM D7913	17.1 MPa (2.48 ksi)	1.7 MPa (0.25 ksi)

2.2. *Test specimens*

The study consisted of sixteen (16) GFRP concrete beams, each measuring 300 mm (11.8 in.) wide, 440 mm (17.3 in.) deep and 5200 mm (205 in.) long (4800 mm (189 in.) span long). M13 (No.4) GFRP stirrups, spaced 125 mm (5 in.) center to center, were used within the shear span length to prevent shear failure. M10 (No.3) steel rebars were used as top reinforcement to support the cage. However, they were cut at the point of load application to avoid any disturbances in the constant moment zone under assessment. A single M16 (No.5) GFRP sand-coated bar was employed as the longitudinal main reinforcement to achieve a tension-controlled section, characterized by the FRP rupture failure mode. This ensured that the rebar could reach its full tensile strength prior to failure.

Two different concrete clear covers, 38 mm (1.5 in.) and 19 mm (0.75 in.), were selected to evaluate their impact on the bond strength and their influence in the bond failure mode. These values represent the minimum clear cover requirements for a beam and a slab member in accordance with ACI 440.11 [7], respectively. Three different lap splices (i.e., 40-, 60- and 80-times bar diameter) were selected based on the available literature (considering studies that indicated the current equation for development length is over-conservative). The spliced lengths were of 630 mm (25 in.), 950 mm (37.5 in.) and 1270 mm (50 in.), respectively. To enhance reliability and reduce potential discrepancies during analysis, each combination was replicated twice, thereby mitigating the impact of some external parameter. In summary, a total of eight distinct combinations were assessed, and their specifics are provided in Table 4. A standard nomenclature (i.e., *XX-YY(R)*) was employed for labeling each specimen. The first term, XX, represents the splice length (i.e., CC (un-spliced), 40, 60, and 80). The second term, YY, signifies the concrete clear cover (i.e., 0.7 for 19 mm and 1.5 for 38 mm clear cover), and finally, 'R' indicates the first or second repetition. For example, CC-1.5(2) corresponds to the second repetition of an un-spliced rebar specimen with a 38 mm (1.5 in.) clear cover.

Fig. 1 present the reinforcement details and dimensions of a specimen with a splice length of $60d_b$ and 38 mm (1.5 in.) of clear cover (i.e.,

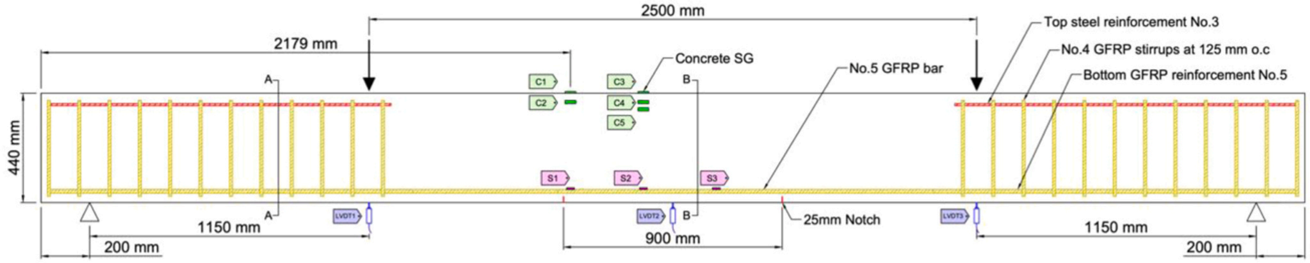

a) 60-1.5 SPECIMEN - FRONT VIEW

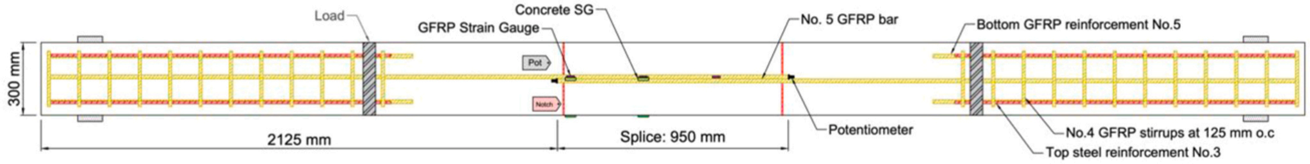

b) DETAILS AND DIMENSIONS - TOP VIEW

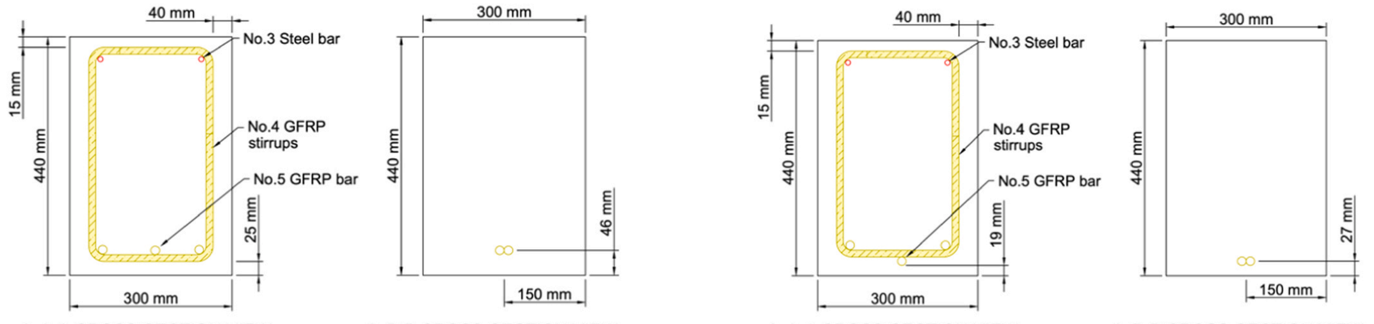

c) A-A CROSS-SECTION VIEW

d) B-B CROSS-SECTION VIEW

e) A-A CROSS-SECTION VIEW 19 mm CLEAR COVER

d) B-B CROSS-SECTION VIEW 19 mm CLEAR COVER

Fig. 1. Reinforcement details of a $60d_b$ specimen with 38 mm (1.5 in.) clear cover; (a) front view; (b) top view; (c) A-A cross-section view; (d) B-B cross-section view; (e) A-A cross-section for 19 mm clear cover and (f) B-B cross-section for a 19 mm clear cover.

60–1.5 specimen) while all other specimens remain identical except for the variation in splice length and clear cover. Furthermore, Fig. 1(e) and (f) show the cross-section view of a 19 mm (0.75 in.) clear cover specimen. Notably, the main rebar had to be positioned below the stirrups to achieve the desired concrete cover. This arrangement was made based on construction considerations, as the stirrups were exclusively employed to prevent shear failure within the shear span zone and were not employed as confinement reinforcement.

2.3. *Theoretical capacity*

Based on the provided data, the theoretical cracking moment, design moment, and theoretical ultimate moment were computed following ACI 440.11–22 provisions [7]. The main distinction between the calculations lay in the utilization of design factors for computing the design moment (ϕMn), including the employment of the environmental reduction factor (C_E), strength reduction factor (ϕ), and the utilization of the guaranteed tensile strength (f_{fu}*). In contrast, when determining the ultimate theoretical moment, these factors were not taken into consideration. Instead, the average ultimate tensile strength (f_u) derived from testing was employed, with no influence from its standard deviation (σ). Note: the guaranteed tensile strength (f_{fu}*) is typically calculated as the ultimate tensile strength (f_u) minus three times the standard deviation (σ). To develop the full capacity of the GFRP rebar, a tension-controlled section design was required (FRP rupture prior concrete crushing). In chapter 22.3.1.1 of ACI 440.11–22 [7], a commentary addresses sections where the design is controlled by the GFRP rupture limit state. Two design approaches are possible. The first involves a simplified and conservative estimation of the nominal flexural strength based on force equilibrium and strain compatibility, assuming the neutral axis equals the balanced neutral axis. The second approach entails a more precise computation of the neutral axis depth. For the present calculation, the Todeschini Stress-Block method was chosen, requiring an iterative procedure to determine the concrete stress and neutral axis depth [3]. Since the section was tension-controlled, a strength reduction factor of 0.55 was utilized.

After multiple iterations, an theoretical ultimate moment (Mth) of 105 kN·m and 100 kN·m was determined for the 19 mm and 38 mm clear cover specimens (19 mm-cc and 38 mm-cc from now on for simplicity), respectively. Table 2 depicts the theoretical and design moment for each group of specimens, with a computed design moment (ϕMn_{lab}) of 46 kN·m and 44 kN·m, respectively. It is worth mentioning that this design moment was computed based on the guaranteed tensile strength from the laboratory tests ($f_{fu}* = 1238$ MPa, as seen in Table 1). If the reference for this value were taken from ASTM D8505 [8], a minimum guaranteed tensile strength of 912 MPa (132 ksi) could be computed based on Table 3 of the standard. This computation resulted in a design moment (ϕMn_{D8505}) of 34 kN·m and 33 kN·m, respectively, which was 25% smaller than the one computed using the laboratory value.

2.3.1. *Development length requirements*

The required development length (l_d) for a M16 (No.5) GFRP rebar was computed based on ACI 440.11–22 chapter 25.4.2 [7] and shown in Eq. (1).

Table 2

Theoretical capacity and design moment.

Specimen	Theoretical Ultimate Moment (Mth)	Design Moment (ϕMn_{lab})	Design Moment (ϕMn_{D8505})
19 mm (0.75 in.) clear cover	105 kN·m (77.4 kip·ft)	46 kN·m (33.9 kip·ft)	34 kN·m (25.1 kip·ft)
38 mm (1.50 in.) clear cover	100 kN·m (73.8 kip·ft)	44 kN·m (32.5 kip·ft)	33 kN·m (24.3 kip·ft)

Table 3

Development length requirements.

Specimen	l_D [Eq. (2)]	l_d [Eq. (1)]	Lap Splice Length (l_s)
	Wambeke and Shield [12]	*ACI 440.11–22* [7]	
19 mm (0.75 in.) clear cover	118d$_b$ or 1.88 m (74 in.)	108d$_b$ or 1.72 m (68 in.)	140d$_b$ or 2.23 m (88 in.)
38 mm (1.50 in.) clear cover	109d$_b$ or 1.73 m (69 in.)	100d$_b$ or 1.59 m (63 in.)	130d$_b$ or 2.07 m (82 in.)

$$l_d = \frac{\left(\frac{f_{fr}}{0.083\sqrt{f'_c}} - 340\right)\Psi_t}{13.6 + \frac{c_b}{d_b}} d_b(SI) \tag{1}$$

Where: f_{fr} = Stress in the bar required to develop the full nominal sectional capacity (MPa). It is equal to f_{fu} for tension-controlled designs and is less than f_{fu} for any other case. f_{fu} = Design tensile strength of GFRP longitudinal reinforcement (MPa), equal to the environmental factor (C_E) times the guaranteed tensile strength (f_{fu}*). c_b = Lesser of the distance from center of a bar to nearest concrete surface, and one-half the center-to-center spacing of bars being developed (mm). The ratio between c_b and d_b shall not be taken greater than 3.5. ψ_t = Factor used to modify development length for casting location in tension. It shall be 1.5 if more than 305 mm (12 in.) of fresh concrete is placed below horizontal reinforcement being developed and 1.0 for all other cases. f_u = Mean tensile strength of sample of test specimens (MPa). The values of $\sqrt{f'_c}$ shall not exceed 8 MPa or 100 psi. Furthermore, the initial equation, formulated by Wambeke and Shield [12] and presented in Eq. (2), was employed to calculate the spliced length required to achieve the complete rebar capacity. This equation was based on 75 beams tests that presented a splitting failure mode and consisted of beam end tests, notched beam tests, and splice tests.

$$l_D = \frac{\left(\frac{f_u}{0.33\sqrt{f'_c}} - 100\right)}{4.0 + 0.3\frac{c_b}{d_b}} d_b(SI) \tag{2}$$

Table 3 presents the development and splice length requirements based on the above equations. An embedment length of 118d$_b$ and 109d$_b$ was required to reach the full capacity of the M16 (No.5) GFRP bar (Eq. (2)) in the 19 mm-cc and 38 mm-cc specimens, respectively. This length was reduced to 108d$_b$ and 100d$_b$, respectively, when working with ACI 440.11–22 requirements (Eq. (1)), such as the implementation of the environmental factor (C_E) and the guaranteed tensile strength (f_{fu}*). These factors, which limit the capacity of the GFRP rebar, resulted in an 8.4% reduction in the required length. Furthermore, chapter 25.5.2.1 establishes lap splice lengths (l_s) for GFRP bars in tension, which should be the greater of 1.3 l$_d$, 20d$_b$ and 305 mm (12 in.) for Class B splice types. The 1.3 factor is used to encourage designers to stagger the location of splices and locate the splice away from regions of high tensile stress. In this case, the splice length should be 140d$_b$ and 130d$_b$, respectively. This factor represented an increment of 19% from the original expression (Eq. (2)). In the present study, the assessed lap splice lengths are, on average, 30%, 46% and 61% of the lap splice length requirements (l_s) for the 40d$_b$, 60d$_b$ and 80d$_b$ specimens, respectively. In terms of development length (l_d), the 40d$_b$, 60d$_b$, and 80d$_b$ specimens represent 39%, 60% and 79% of l_d, respectively.

2.4. *Test setup and Instrumentation*

The four-point-bending beams were tested utilizing a displacement control protocol (at a rate of 1.2 mm/min (0.047 in/min)) encompassing three cycles. In the initial cycle, the beams were subjected to loading up to 1.15 times the computed cracking load. Moving to the second cycle, loading continued until reaching the calculated design load or until a rebar slippage of 0.5 mm (0.02 in.) occurred, whichever came first (this slippage criterion was selected based on a review of relevant literature as a reference for rebar movement [10]). Finally, the third cycle progressed until the beams reached failure. Prior to testing, a notch was made in each beam near the splice end, aiming to induce main cracks specifically at the splice location (refer to Fig. 1 for visualization). The notch dimensions were governed by the blade thickness, beam width, and a depth of either 12 mm (0.47 in.) or 25 mm (1 in.), based on the concrete clear cover (i.e., for 19 mm-cc and 38 mm-cc specimens, respectively). For context, the schematic setup of the four-point bending test is illustrated in Fig. 2.

Throughout the testing process, comprehensive data on load, strains (for both reinforcement and concrete), and deflection were systematically gathered. This data acquisition aimed to evaluate the structural response of the beam specimens. The mid-span deflection was monitored using a linear variable differential transformer (LVDT) located at mid-span and at the points of load application (see Fig. 1). The strains at the concrete and the rebar were recorded using adhesively bonded strain gauges (SG). Three 6 mm (0.24 in.) gauge length, strain gauges were located along the length of the rebar (prior to the casting of the beam). The first strain gauge was installed 50 mm (2 in.) inside the splice end (as shown in Fig. 1), the remaining two were evenly positioned along the splice length, maintaining an equidistant separation corresponding to one-third of the splice length. When installing the strain gauges, efforts were made to minimize any disturbance to the sand coating treatment (see Fig. 3(a)), as the surface needed to be ground at the location point, which affects the bond strength of the rebar. This consideration led to the decision of installing only three strain gauges along the length of the rebar. Finally, five 60 mm (2.4 in.) gauge length, strain gauges were placed on the upper part of the beams (once the concrete was hardened and the beams were ready to be tested) to check the compressive strains in the concrete. The strain gauges in the concrete were positioned at the same distance as the strain gauges on the rebar. Two were placed on the upper face of the beam, an additional two were situated on one side, 30 mm from the surface, and a final SG was located 60 mm from the upper surface (see Fig. 3(b)). All measuring devices were connected to an independent multi-port data acquisition system.

In addition, a small potentiometer was positioned at the center of the rebar cross-section to measure relative slip. The procedure employed was both straightforward and effective. A small hole was drilled at the center of the rebar, with ample tolerance to accommodate the potentiometer shaft (see Fig. 4). Before inserting the shaft into the hole, resin was carefully applied to ensure good adherence. Finally, the potentiometer was covered with a heat shrink tube to avoid potential damage during concrete pouring and to ensure its stability. Once the reinforcement cage was positioned within the formwork, the potentiometer was securely fastened to prevent any movement along with the rebar.

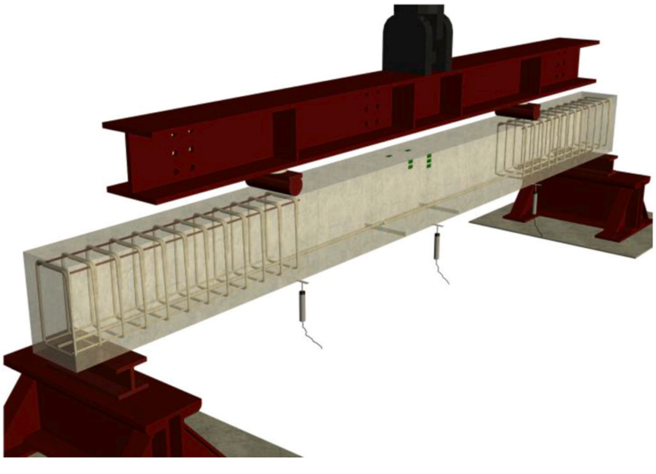

Fig. 2. Schematic setup of the four-point bending test.

3. Experimental Results and Discussion

Table 4 presents the results obtained from the four-point bending tests. The table includes the theoretical and test moment, the mid-span deflection, the ratio between the test and the theoretical moment, the ratio between the test and the design moment as per ACI 440.11–22, and the failure mode for each specimen.

3.1. *Structural behavior and failure mode*

3.1.1. *Control beams (CC-0.7 and CC-1.5)*

Remarkably, the un-spliced GFRP-RC specimens achieved load capacities that closely approached the theoretically ultimate value (Mth), with an average test-to-theoretical moment ratio of 0.96 and 0.99 for CC-0.7 and CC-1.5, respectively, showing the accuracy of the design approach (see Fig. 8 for reference). Furthermore, the overall average test-to-design moment ratio of 2.22 (122% higher) highlighted the inherent conservatism prescribed by the design codes. While originally designed as an under-reinforced member expected to fail through "FRP rupture", the specimens experienced failure due to concrete crushing near the point of load application as shown in Fig. 5. However, upon analyzing the strain gauges positioned near the notches on the bar, a maximum strain of approximately 0.0198, equivalent to 97% of the ultimate tensile strain, was observed, indicating that the bar was close to rupture. Approximately six major flexural cracks were formed along the constant moment zone. The initial group of cracks at notches (the un-spliced specimens were notched similarly to the 40d_b specimens) appeared at a moment of 20 kN·m (14.8 kip·ft). As the load increased, the cracks grew in width and propagated towards the upper face of the beam (the design neutral axis was 35 mm (1.38 in.) and 39 mm (1.53 in.) for the 19 mm-cc and 38 mm-cc specimens, respectively). Fig. 5 displays the mode of failure of un-spliced specimens. A 90 mm (3.5 in.) red grid was marked within the constant-moment zone for reference.

3.1.2. *Spliced beams with 19 mm clear cover (40–0.7, 60–0.7 and 80–0.7)*

Fig. 6 illustrates the failure mode and crack patterns observed in spliced specimens with 19 mm (0.75 in.) concrete clear cover. Notably, all specimens failed prior to reaching the theoretical capacity (see Fig. 8). The initial group of cracks appeared at the notches, occurring at an approximate moment of 26 kN·m (19.2 kip·ft), and then widened while propagating toward the upper face of the beam. This led to the failure mode of the beams being classified as splitting, attributed to a distinct bottom crack running along the length of the splice. This crack significantly influenced the stress transfer mechanism, consequently reducing the overall load-bearing capacity of the beam. When compared to the un-spliced specimens where six distinctive flexural cracks formed, the 40d_b-0.7 specimens exhibited only three cracks in the constant moment region, highlighting the inadequate splice length to transfer the stresses between the rebars and back to the concrete. Similarly, the 60d_b-0.7 specimens displayed five cracks before failure, with the main crack notably at the left notch. Meanwhile, the 80d_b-0.7 specimens developed six cracks, with the main cracks at the notch. Although the latter specimens mirrored the crack number of un-spliced ones, it is evident that they were not uniform, and the splice end location acted as a weak point impacting the capacity of the beam.

Fig. 8 presents the comparison between test- and theoretical-moment. 40d_b-0.7 specimens failed to meet the design moment, reaching only, on average, 81% of ϕMn. However, 60d_b-0.7 and 80d_b-0.7 specimens, exceeded this value by an average of 10% and 26%, respectively. Reaffirming the conservatism of the design philosophy. An average capacity moment (Mtest) of 55%, 48%, and 35% Mth for the

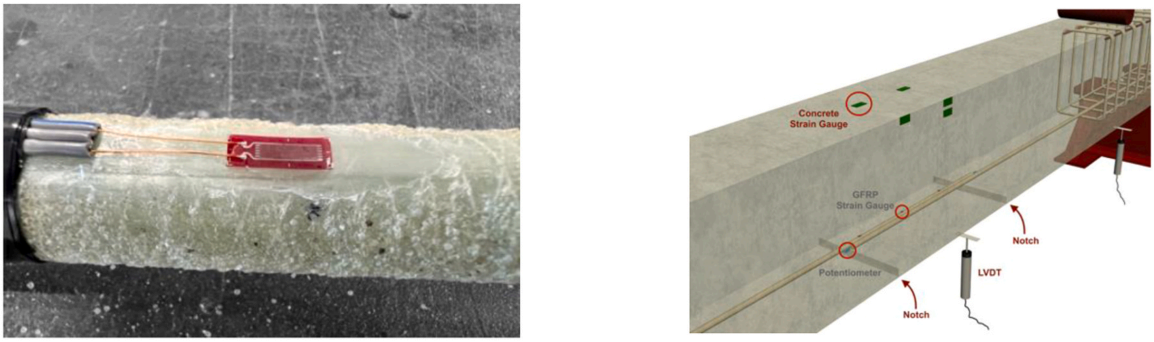

(a) (b)

Fig. 3. Instrumentation (a) Strain gauges installation; (b) Instrumentation detailing.

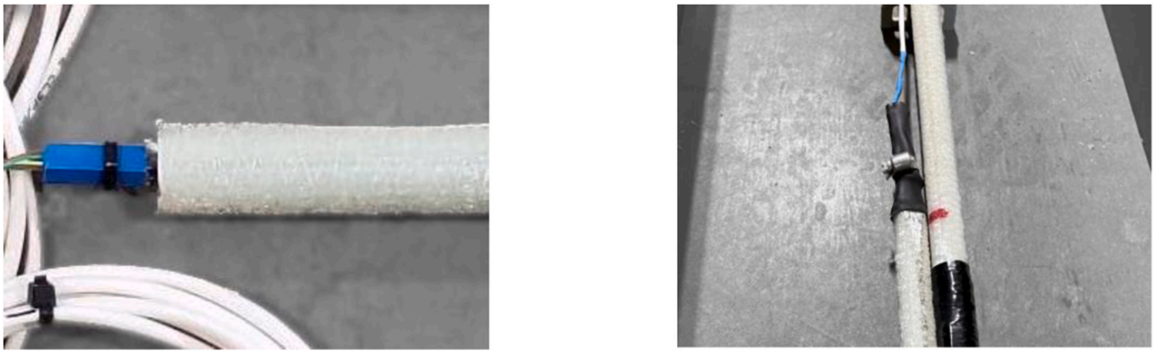

(a) (b)

Fig. 4. Potentiometer installation (a) in rebar; (b) with heat shrink tube.

Table 4
Specimen details and test results.

Specimen	Splice Length (mm)	f'c (MPa)	Theoretical Moment (Mth) (kN·m)	Test Moment (Mtest) (kN·m)	Mid-span deflection (mm)	Mtest / Mth	Mtest / ϕMn	Failure mode
CC-0.7(1)	un-spliced	35.5	105	102	151	0.97	2.21	Concrete crushing
CC-0.7(2)	un-spliced	35.5	105	99	147	0.94	2.16	Concrete crushing
80–0.7(1)	1270	40.0	106	59	76	0.56	1.29	Splitting
80–0.7(2)	1270	43.5	106	56	55	0.53	1.23	Splitting
60–0.7(1)	950	43.0	106	46	48	0.44	1.01	Splitting
60–0.7(2)	950	42.1	106	55	64	0.52	1.19	Splitting
40–0.7(1)	630	40.0	106	42	40	0.39	0.90	Splitting
40–0.7(2)	630	42.1	106	33	26	0.31	0.72	Splitting
CC-1.5(1)	un-spliced	35.5	100	101	147	1.01	2.30	Concrete crushing
CC-1.5(2)	un-spliced	36.0	100	96	131	0.96	2.19	Concrete crushing
80–1.5(1)	1270	42.1	101	67	66	0.67	1.53	Splitting
80–1.5(2)	1270	43.5	101	73	78	0.72	1.65	Splitting
60–1.5(1)	950	43.0	101	57	65	0.56	1.29	Splitting
60–1.5(2)	950	43.0	101	61	72	0.61	1.39	Splitting
40–1.5(1)	630	40.0	101	45	40	0.45	1.03	Splitting
40–1.5(2)	630	43.5	101	47	46	0.46	1.06	Splitting

Note: All measurements are provided in their respective SI units, with the following conversions for reference: mm to inches: divide by 25.4; MPa to psi: multiply by 145.04; kN·m to kip·ft: multiply by 0.738.

$80d_b$-0.7, $60d_b$-0.7, and $40d_b$-0.7 specimens, respectively, was recorded. In summary, a reduction of 42%, 56% and 71% from the required lap splice length (i.e., $140d_b$) resulted in reductions of 45%, 52% and 65% in the moment capacity. The variability in the tests of similar characteristics could be explained by the cracking formation pattern. The specimens that failed with a lower load exhibited cracks closer to each other, possibly indicating weak locations where stress was being transferred. Further studies on bond transfer mechanisms are required.

3.1.3. Spliced beams with 38 mm clear cover (40–1.5, 60–1.5 and 80–1.5)

The failure mode observed in all 38 mm concrete clear cover spliced specimens was splitting, where a bottom crack form along the length of the lap splice leading to a separation of the surrounding concrete from the rebar, resulting in a loss of bearing capacity for the beam member. Fig. 7 illustrates the failure mode and crack patterns observed in the spliced 38 mm-cc specimens. All specimens failed prior to reaching the theoretical capacity as shown in Fig. 8. The initial group of cracks appeared at the notches, occurring at an approximate moment of 26 kN·m (19.2 kip·ft), and then widened while propagating toward the

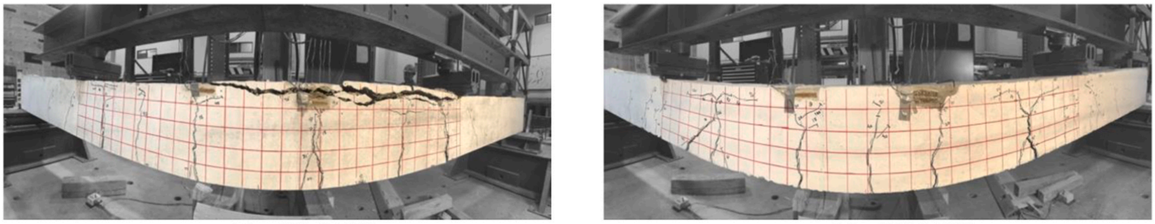

(a) CC-0.7(1) (b) CC-0.7(2)

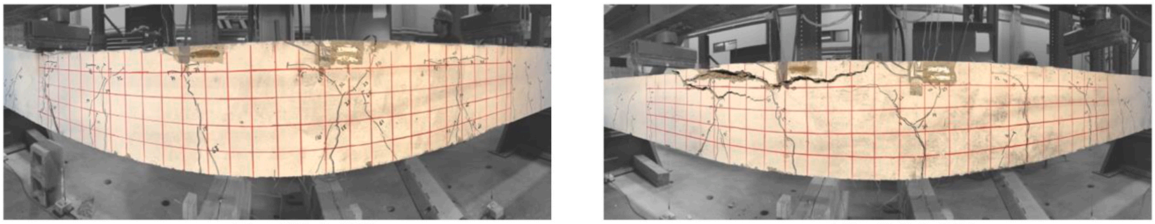

(c) CC-1.5(1) (d) CC-1.5(2)

Fig. 5. Failure mode of un-spliced specimens.

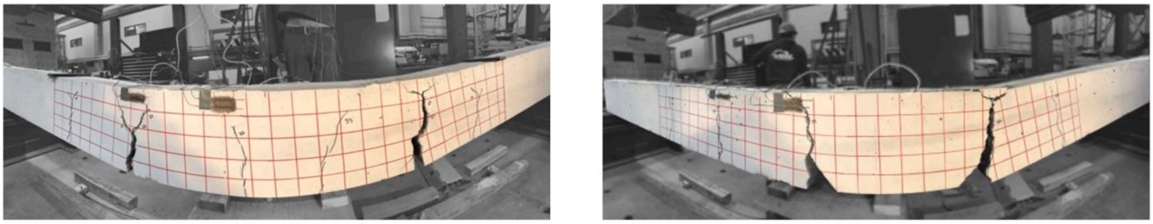

(a) 80-0.7(1) (b) 80-0.7(2)

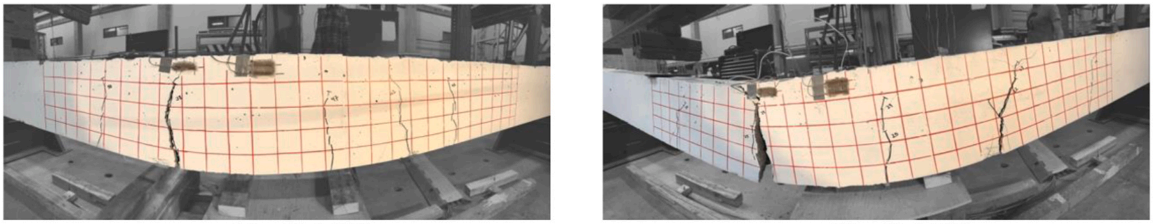

(c) 60-0.7(1) (d) 60-0.7(2)

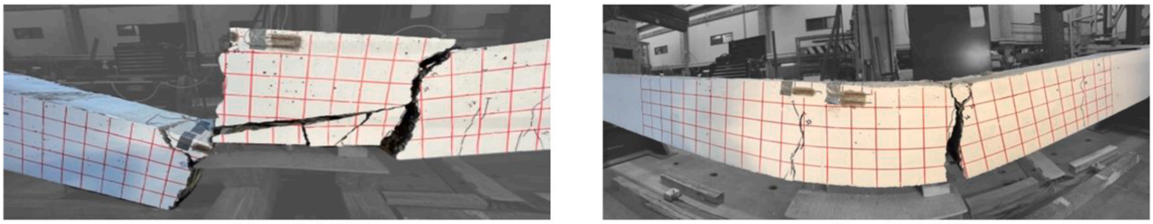

(e) 40-0.7(1) (f) 40-0.7(2)

Fig. 6. Failure mode of spliced specimens with 19 mm of concrete clear cover.

upper face of the beam. The crack pattern was similar to that of 19 mm-cc specimens, showing the main influence of the lap splice length. From Fig. 8, it can be appreciated that in average all specimens reached the design moment capacity with 80d$_b$-1.5, 60d$_b$-1.5 and 40d$_b$-1.5 specimens exceeding this value by an average of 59%, 34% and 5%, respectively. An average test moment (Mtest) of 70%, 58%, and 46% Mth for 80d$_b$-1.5, 60d$_b$-1.5, and 40d$_b$-1.5 specimens respectively, was recorded. In summary, a reduction of 36%, 52% and 69% from the required lap splice length (i.e., 130d$_b$) resulted in reductions of 30%, 42% and 54% in the moment capacity.

3.2. Moment-deflection curves

Fig. 9 presents the mid-span moment vs deflection curve for all the different combinations (note: for the sake of discussion and analysis simplicity, and due to structural behavior similarity, repetitions per combination were averaged into a single specimen; the absence of brackets signifies average values. Additionally, the unloading stages were removed). A bilinear behavior with an initial stage up to the cracking moment, where the concrete controls the stiffness of the specimen, can be observed, this is followed by a noticeable drop in stiffness upon cracking of the specimen that continue linear up to failure. The load-bearing capacity of the spliced specimens was affected, while the stiffness of the beam appeared to remain unaltered by the splitting

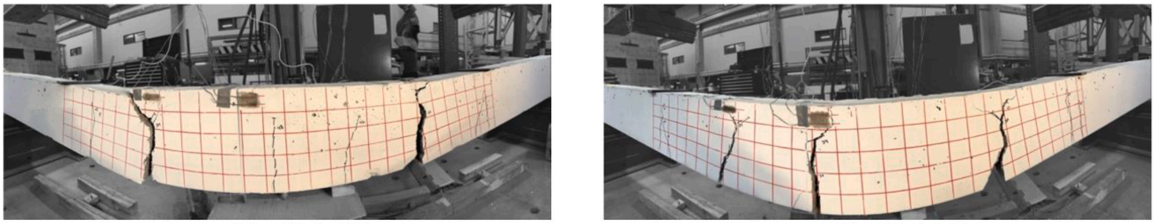

(a) 80-1.5(1)

(b) 80-1.5(2)

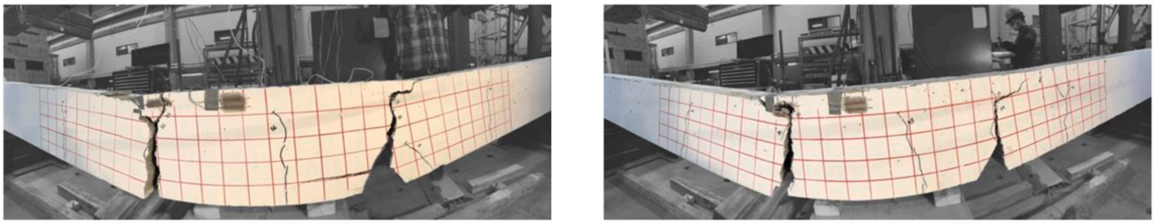

(c) 60-1.5(1)

(d) 60-1.5(2)

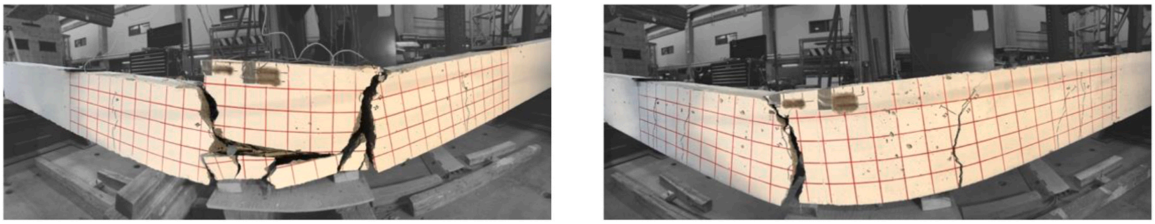

Fig. 7. Failure mode of spliced specimens with 38 mm of concrete clear cover.

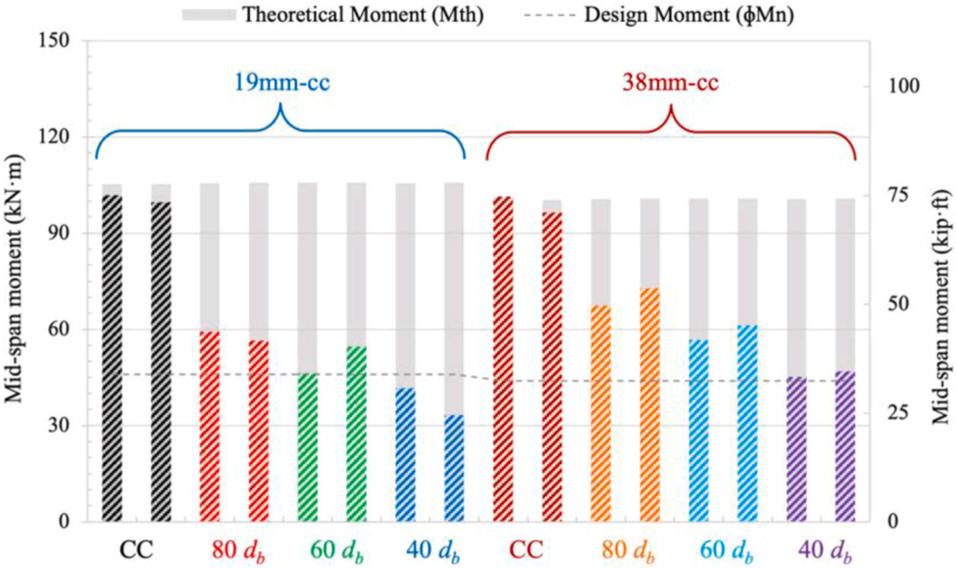

Fig. 8. Comparison between test- and theoretical- moment.

failure mode. Despite maintaining the same slope, the specimens exhibited a brittle failure. These findings are in agreement with the results reported by Zemour et al. [21] and Pay et al. [23], who confirmed the accuracy of flexural-theory methods in evaluating tensile stresses. By knowing the moment capacity of the lap-spliced beam, the stress in the rebar can be found with a moment-curvature analysis.

One might have anticipated greater deflection in the lap-spliced specimens due to the potential for rebar slippage and the widening of the main crack. However, it appears that, despite differences in crack distribution compared to the un-spliced specimen, the nonuniform crack pattern still resulted in a similar level of deflection when subjected to the same applied load. In a scenario involving bond failure, the beam specimen may not exhibit excessive deflection as an early indicator of design failure. Warning signs of bond failure would manifest as localized cracks at the lap splice end, distinguishable by their wider width compared to the other cracks distributed along the beam. In the case of the 19 mm-cc specimens, reductions of 42%, 56%, and 71% from the required lap splice length (i.e., 140d_b) resulted in reductions of 56%, 62%, and 78% in the maximum mid-span deflection of the un-spliced specimen (i.e., 150 mm or 5.9 in.). Conversely, a reduction of 36%, 52%, and 69% from the required lap splice length (i.e., 130d_b) in the 38 mm-cc specimens led to reductions of 48%, 51%, and 69% in the

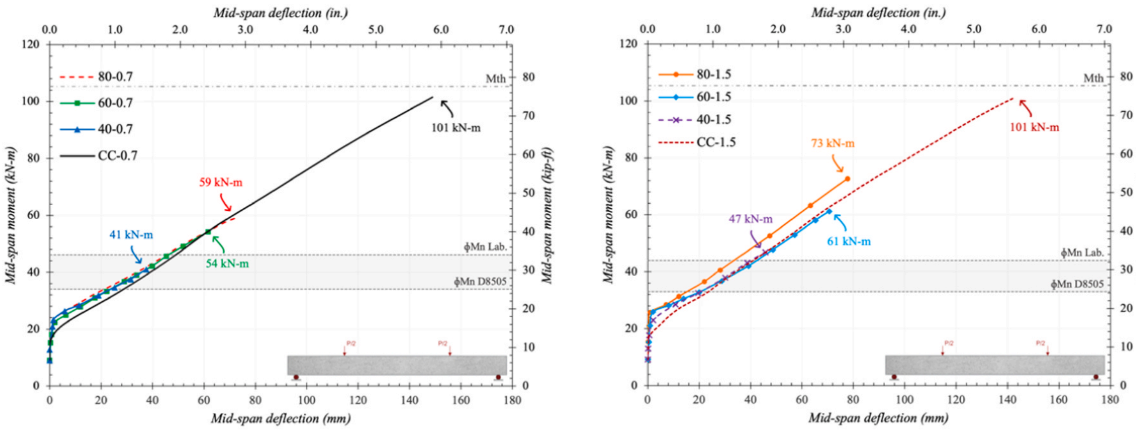

(a) 19 mm (0.75 in.) clear cover specimens (b) 38 mm (1.5 in.) clear cover specimens

Fig. 9. Mid-span moment vs. deflection.

maximum mid-span deflection of the un-spliced specimen (i.e., 140 mm or 5.5 in.). Although the 38 mm-cc specimens exhibited higher deflection at failure, this deflection did not result in a reduction of load-bearing capacity. Both combinations exhibited similar deflection values for a given applied load.

3.3. *Rebar strain*

During the beam test, rebar strain was recorded to analyze stress transfer along the lap splice length and measure the maximum tensile stress before failure. However, many of the rebar strain gauges (SG) failed during the test, and no maximum strain values were recorded. One approach to recover this data involved projecting the slope before strain gauge failure, taking advantage of the elastic-up-up-failure nature of the

Table 5
Experimental and predicted values of bond strength.

Specimen	Recorded Strain (ε_r) (mm/mm)	Todeschini Strain (ε_t) (mm/mm)	Splice Strength (f_{test}) (MPa)	Average Bond Strength (μ_{avg}) (MPa)	ACI 440 Bond Stress (μ_{ACI}) (MPa)	μ_{ACI} / μ_{avg}	CSA S806-12 (μ_{S806}) (MPa)	CSA S6-19 ($\mu_{S6\text{-}19}$) (MPa)
CC-0.7 (1)	0.021*	0.020	1279[†]	-	-	-	-	-
CC-0.7 (2)	0.020*	0.019	1248[†]	-	-	-	-	-
80–0.7 (1)	n/a	0.011	732	2.3	3.0	1.321	2.9	2.4
80–0.7 (2)	n/a	0.011	700	2.2	3.2	1.443	2.9	2.5
60–0.7 (1)	n/a	0.009	573	2.4	3.4	1.409	2.9	2.5
60–0.7 (2)	0.011*	0.010	678	2.8	3.3	1.177	2.9	2.5
40–0.7 (1)	n/a	0.008	513	3.2	3.7	1.148	2.9	2.4
40–0.7 (2)	n/a	0.008	513	2.6	3.8	1.476	2.9	2.5
CC-1.5 (1)	0.020*	0.021	1341[†]	-	-	-	-	-
CC-1.5 (2)	0.020*	0.020	1274[†]	-	-	-	-	-
80–1.5 (1)	0.014*	0.014	880	2.8	3.3	1.198	4.3	3.7
80–1.5 (2)	n/a	0.015	951	3.0	3.4	1.127	4.3	3.7
60–1.5 (1)	0.010*	0.011	733	3.1	3.6	1.165	4.3	3.7
60–1.5 (2)	0.016*	0.012	797	3.3	3.6	1.071	4.3	3.7
40–1.5 (1)	0.008*	0.009	590	3.7	3.9	1.049	4.3	3.6
40–1.5 (2)	0.013*	0.009	606	3.8	4.0	1.064	4.3	3.7

Note: All measurements are provided in their respective SI units, with the following conversions for reference: mm to inches: divide by 25.4; MPa to psi: multiply by 145.04.

* The rebar strain values were projected based on the same slope of the curve up to the failure point.

[†] These values do not represent a lap splice strength but serve as a reference for the maximum stress in the un-spliced rebar.

GFRP rebar. The values derived from this projection are presented in the second column of Table 5. Another method, based on prior studies [21, 23,30,38], employed a moment-curvature analysis using the moment capacity of the beam as a reference. The Todeschini stress-strain curve was used in this case, and the resulting values are also shown in Table 5. It is worth mentioning that, as stated by Pay et al. [23], the values obtained from the moment-curvature analysis closely aligned with those found using the cracked section analysis.

Fig. 10 presents the variation of tensile strain of the rebar along the lap splice length for the 19 mm-cc specimens (It is noteworthy that the decision to install strain gauges on the rebar could have influenced the bond strength of the specimen. This is due to the waterproofing protection and the removal of the sand-coated treatment, which created a ’bond breaker,’ likely impacting its performance. The 40db specimens experienced the highest impact, resulting in an 11% effect on the perimeter area). As mentioned earlier, three strain gauges were installed in the rebar to measure strain variations, with the ’0’ location positioned 25 mm (1 in.) inside the notch. The graphs illustrate how this variation changes as the applied moment increases, with steps defined by a percentage of the theoretical moment (i.e., Mth = 105 kN·m or 77.4 kip·ft). With increasing load, a non-linear stress distribution along the splice becomes evident. This can be attributed to the initiation of beam cracking, where stresses begin to transfer between the bars and back to the concrete. As cracks develop along the splice and loads increase, it can be expected that the stresses between the cracks or gauges become uniform since there is not sufficient length to transfer them back to the concrete. Therefore, this change in stresses could be attributed to stress transfer between the bars and minimal transfer to the concrete. This observation is consistent with Abbas et al. [10], who found that the strain distribution along the lap splice zone appeared to be linear in specimens without confinement. In contrast, Makhmalbaf and Razaqpur [16] found that the strain distribution along the embedment length in a hinged beam followed a modified form of the logistic growth function, particularly concerning the distribution of stresses back to the concrete.

3.4. *Influence of parameters*

Theoretically, the ultimate theoretical moment of the 19 mm-cc lap-spliced specimens was higher than the 38 mm-cc specimens due to their longer effective depth. In fact, the un-spliced 19 mm-cc specimens reached a higher ultimate moment than the 38 mm-cc ones. However, the smaller effective cover (the distance from the center of the rebar to the outer tensile fiber) made them more susceptible to splitting cracks. Consequently, the 38 mm-cc specimens exhibited a greater load-bearing capacity before failure, on average 21% higher than the 19 mm-cc specimens. The impact of the concrete clear cover was evident but there were not enough data points to correlate the changes in capacity. Fig. 11 illustrates the relationship between the lap splice length and the moment capacity (Mtest) to theoretical capacity (Mth) ratio. When comparing the increase in moment capacity due to increments in lap splice length, and assuming a linear relationship, an average increment ratio of 0.39 kN·m per cm (0.73 kip·ft per in.) was observed. Although linearity in this increment cannot be assured after 80d_b, its assumption serves to uphold a conservative approach.

The 38 mm-cc specimens exhibit a clearer trend, beginning at a 20% Mtest/Mth, which closely aligns with the average cracking moment. Assuming this linear trend continues, the lap splice length required to achieve 100% capacity aligns with ACI 440.11–22 provisions: 140d_b for 19 mm-cc specimens and 130d_b for 38 mm-cc specimens. Following this trend, the 100% capacity would be attained with lap splice lengths of 153d_b (2.4 m) and 127d_b (2.0 m) for the 19 mm-cc and 38 mm-cc specimens, respectively. Compared to the original expression (Eq. (2)), these lap splice lengths represent a 30% and 17% increment, respectively, indicating that the expression given by Wambeke and Shield [12] is not enough for achieving the full rebar capacity. It is worth noting that most of the beam tests on which the equation was based were hinged and

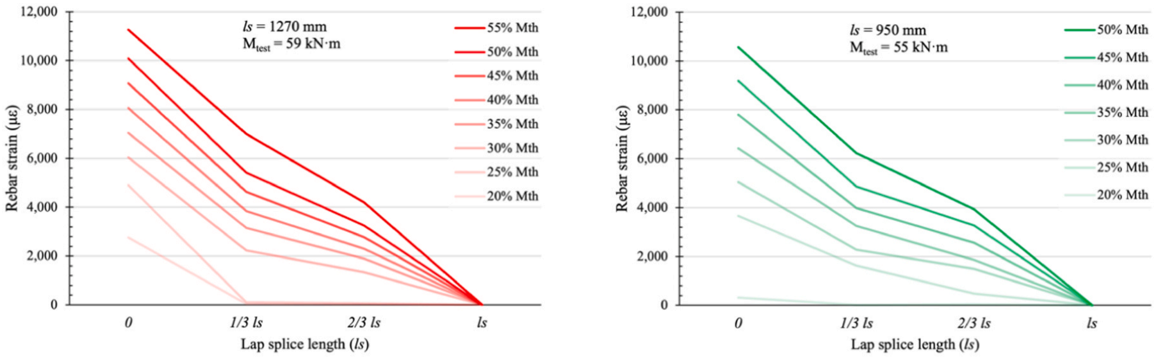

(a) 80-0.7(1) (b) 60-0.7(1)

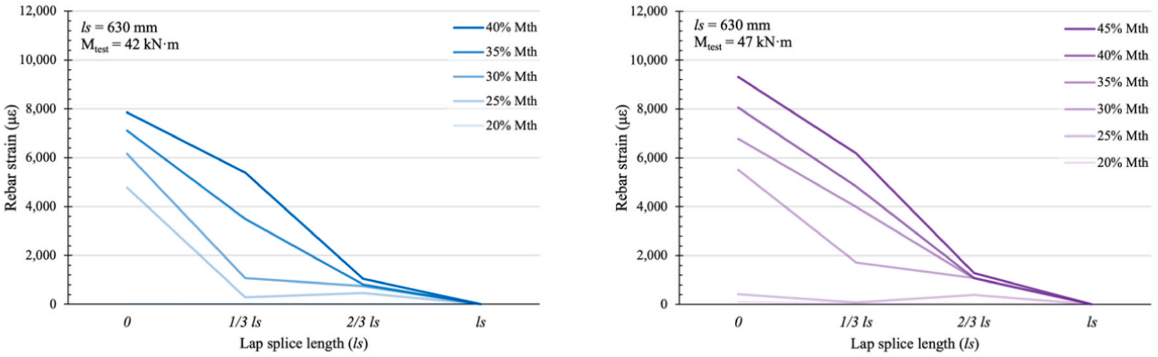

(c) 40-0.7(1) (d) 40-1.5(1)

Fig. 10. Variation of tensile strain along the splice length (19 mm-cc specimens).

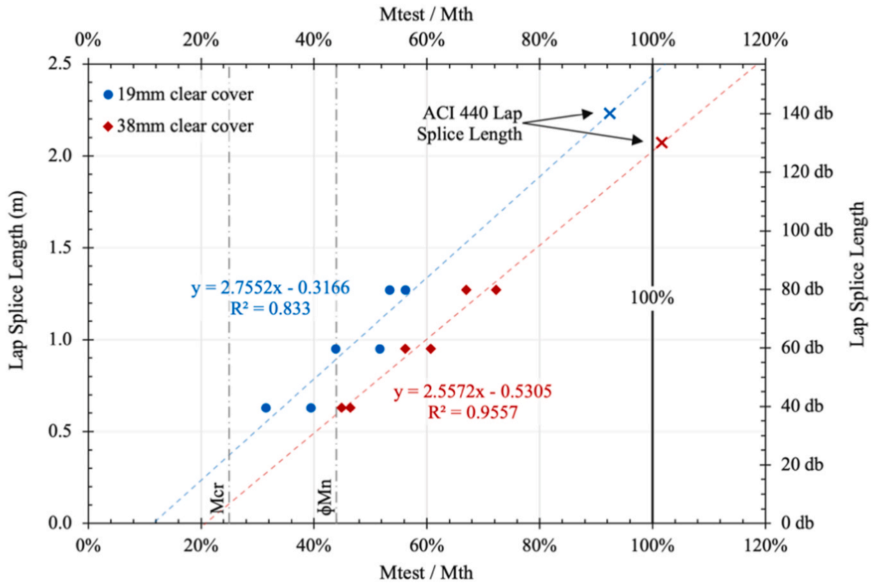

Fig. 11. Relation between the lap splice length and the Mtest to Mth ratio. *Note: The length is provided in its respective SI unit, to convert from m to inches: divide by 0.0254.*

notched beam tests, typically involving a single bar transferring stresses to the concrete without the presence of additional rebars (lap splice scenarios).

Furthermore, 153d$_b$ and 127d$_b$ represent changes of −10% and 2%, respectively, when compared to the ACI 440.11–22 provisions. However, the lap splice length expression in ACI 440.11–22 considers all strength factors (i.e., C$_E$ and f_{fu}*), thereby reducing the capacity of the rebar and not accounting for its full tensile strength. If these factors are considered, the maximum usable capacity would be 80% of Mth, which is the nominal moment (Mn). To reach this capacity, and based on the linear tendency observed, lap splice lengths of 119d$_b$ (1.9 m) and 95d$_b$ (1.5 m) would be required for the 19 mm-cc and 38 mm-cc specimens, respectively. This represents a 15% and 27% reduction from the 140d$_b$ and 130d$_b$ ACI 440.11–22 provisions, respectively.

3.5. Average bond strength

To determine the stress in the GFRP rebar at failure (referred to as "f_{test}") for each beam, the strain at failure (ε_t) was multiplied by the modulus of elasticity of the GFRP bar (E_f). This calculation, also referred to as splice strength, is presented in column 4 of Table 5. The average bond stress, designated as μ_{avg}, was computed by assuming that the tensile force applied to the rebar was countered by a uniform stress distribution across the entire surface of the rebar, as shown in Eq. (3) and recorded in column 5 of Table 5. While non-uniform stress distributions have been proposed by some authors, the general consensus is to assume an average bond stress along the embedded or lap-spliced length, given the multitude of parameters influencing bond distribution.

$$\mu_{avg} = \frac{f_{test} \quad d_b}{4l_e} \tag{3}$$

Fig. 12(a) illustrates the splice strength versus normalized lap splice length for both sets of specimens. The trend shows, on average, a 7% increase in splice strength for every 10d$_b$ increments of lap splice length. The difference between the two groups was significant, with the 38 mm-cc group being 26% higher than the 19 mm-cc group. On the other hand, Fig. 12(b) presents the curve of normalized bond stress versus normalized lap splice length. To account for the variability in concrete compressive strength, the bond stresses were divided by the square root of the concrete compressive strength. The "κ" factor adjusts for the unit system used, with a value of 1 for the inch-pound system and 0.083 for SI units. While various authors have suggested different exponent values,

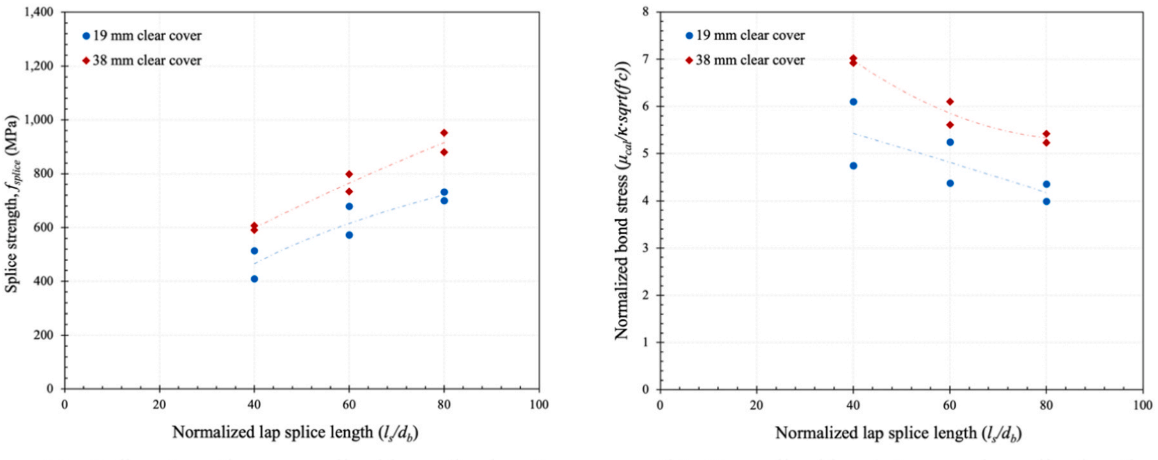

(a) Splice strength vs normalized lap splice length

(b) Normalized bond stress vs. lap splice length

Fig. 12. Comparison between stresses and lap splice length.

including the use of the fourth root of $f'c$, we opted to retain the original approach to facilitate a clear comparison with the current ACI 440.11 expression.

The change in bond stresses did not appear to follow a linear pattern. This behavior could be attributed to the non-uniform distribution of bond stresses along the lap splice length. A longer lap splice length results in higher splice strength, but the increment in splice strength is not proportional. Another contributing factor could be the initiation and propagation of flexural cracks along the lap length. The presence of a flexural crack may indicate that the distance between cracks and the surrounding environment is adequate to transfer tensile stresses back to the concrete, ultimately resulting in crack formation.

3.6. Slippage

The analysis of mid-span moment versus deflection revealed that the bond stresses transfer of the rebar remained unaffected. Fig. 13 illustrates the behavior of the potentiometer installed at the end of the rebar in the one specimen for each combination, demonstrating continuous movement of the rebar after the initial beam cracking. The specimens effectively sustained the applied load throughout. It was anticipated that the member’s stiffness would decrease after rebar slippage, leading to greater deflection. However, the rebar slippage did not significantly impact its bond stress transfer capacity until experiencing a maximum slippage. Nevertheless, it’s essential to note that these findings may not be universally applicable to other specimens, as potentiometer readings suggested smaller slippage values with decreasing splice length, implying potential variations in rebar behavior and bond capacity under different conditions. This suggests that, generally, longer lap splice lengths allow for greater rebar movement before experiencing brittle failure.

Some authors have established maximum slippage values of around 0.254 mm (0.01 in.) when modeling bond strength [10,27]. Saleh et al. [18] observed a bond stress-slip behavior characterized by a substantial initial increase in bond stress, attributed to strong chemical adhesion, without accompanying significant slip. When the chemical adhesion was exhausted, bond stress continued to increase with a slight increase in slip until the peak point. In the present study, due to the larger lap-spliced lengths, the slip after cracking was higher, suggesting that a single maximum bond could not be established even for a specific bar size and surface treatment, because of the large number of parameters impacting the bond behavior.

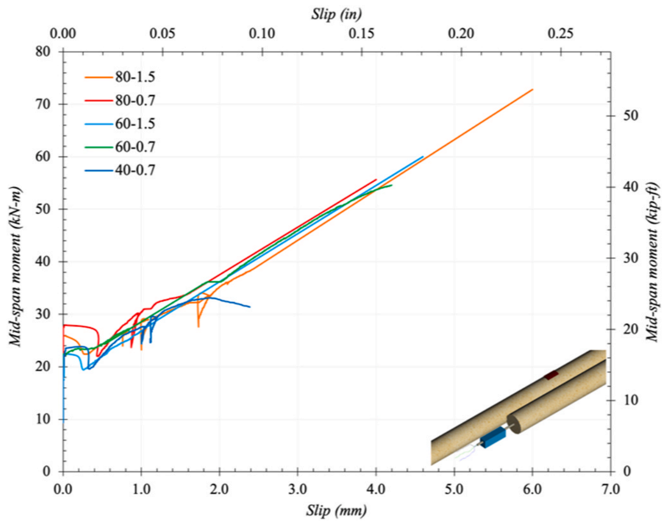

Fig. 13. Mid-span moment vs. Rebar slippage.

4. Comparison with current expressions

The current equation in ACI 440.11–22 code was developed by Wambeke and Shield in 2006. Eqs. (1) and (2) were derived from equating the expression obtained through a linear two-parameter regression analysis (Eq. (4)) to the average bond stress required to develop the full nominal sectional capacity, as represented by Eq. (3) with ’f_{test}’ replaced by ’f_{fu}’. The original expression considered the embedded length in the beam, denoted as ’*le*,’ which in this context corresponds to the lap splice length, ’*ls*.’ The lap splice length requirement, as per ACI 440.11–22, should be equivalent to the development length, ’*ld*,’ typically multiplied by a factor of 1.3. However, the code does not provide an explanation for this factor. The previous document, ACI 440.1R-15, explains that this factor is inherited from ACI 318 for steel reinforcement due to the limited data available for GFRP lap-spliced beams. Furthermore, Tighiouart et al.[39] had proposed a modification factor of 1.3 in 1999 for the bond development length of GFRP bars in order to achieve an adequate tension lap splice length. However, this factor was developed based on the ACI 318–95 equation for steel rebars.

$$\mu_{ACI} = \left[4.0 + 0.3\frac{c_b}{d_b} + 100\frac{d_b}{l_e}\right]\kappa\sqrt{f'_c} \tag{4}$$

Fig. 14 presents the average bond stress versus the lap splice length. Both Eq. (4) and the modified Eq. (3) are depicted in the graph, along with the minimum embedded length required by the ACI provisions to prevent slippage (pull-out) failure. Consequently, three distinct stages can be identified. The first stage, referred to as the ‘slippage’ stage, represents the minimum embedded length required to prevent this failure mode. As previously explained, this should be the greater of 1.3 l_d, 20d_b and 12 in. The second stage is the ‘splitting’ stage, where the expression in Eq. (4) governs the failure mode, and the performance of the beam is controlled by various parameters affecting this expression. Lastly, the point of intersection between Eq. (4) and Eq. (3) should be recognized as the development length, beyond which the GFRP rebar is most likely to fail due to GFRP rupture, with Eq. (3) governing the maximum bond stress. As observed in the graphs, in this case, the intersection of the curves does not coincide with the development length computed using Eq. (1). This discrepancy is attributed to the assumption of $f_{fu}* = 0.85\, f_u$ in the original expression. The GFRP rebars utilized in the present study exhibited higher reliability with $f_{fu}* = 0.93\, f_u$. As a result, the provisions required an increased development length.

The average bond stresses for the 19 mm-cc specimens, as shown in Fig. 14(a), were found to be situated below the expected average bond stresses by the Eq. (4) curve, indicating a less reliable prediction by the expression, with test values averaging 24% lower. In contrast, Fig. 14(b) presents the same comparison for the 38 mm-cc specimens, where a higher prediction can be observed, with test values averaging 10% lower. Additionally, the effect of confinement reinforcement has not been evaluated in this study, which could significantly impact bond strength and reduce the reliability of the expression. Similarly, both embedded lengths and splice lengths should undergo separate analysis to determine the underlying relationship.

In North America, in addition to the ACI 440.11–22 [7] code, there are various bond design equations and guidelines. Canada, for example, provides its own set of guidelines for bond mechanisms, including embedment length and bond strength expressions, as detailed in CSA S806–12 [29] and Chapter 16 of CSA S6–19[40]. This diversity of equations highlights the range of approaches for bond design without a clear consensus on the underlying mechanics. The Canadian Standards Association, CSA S806–12[29], in Chapter 9.3, specifies the Equation (9–1) for calculating the development length of bars in tension. However, no direct equation for bond strength is provided. To demine the average bond strength, Equation (9–1) was equated to Eq. (3) and subsequently solved for the average bond stress (μ_{S806}) in SI units, as

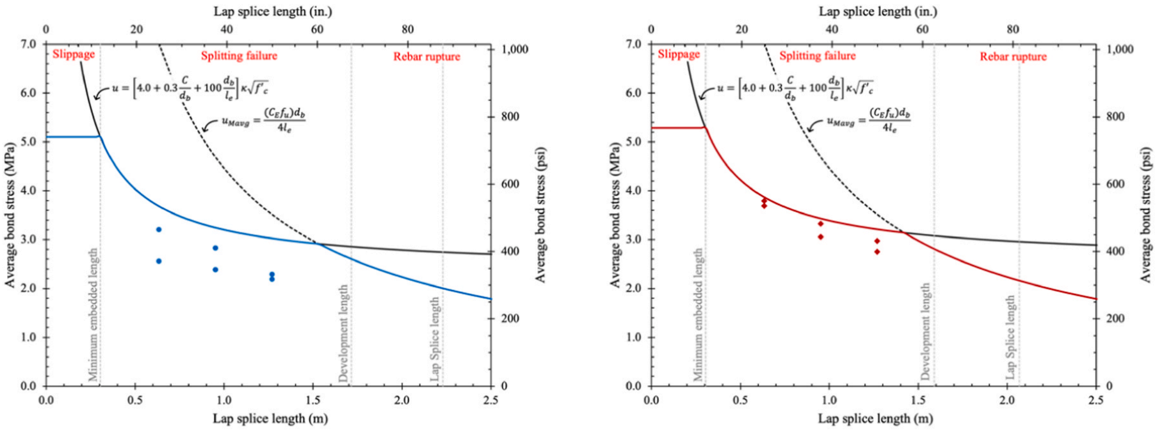

(a) 19 mm (0.75 in.) clear cover specimens

(b) 38 mm (1.5 in.) clear cover specimens

Fig. 14. Average bond stress vs. Lap splice length.

shown in Eq. (5).

$$\mu_{S806} = \frac{d_{cs}\sqrt{f'_c}}{1.15(k_1k_2k_3k_4k_5)\pi d_b} \tag{5}$$

Where, d_{cs} is the smaller of the distance from the center of the bar being developed to the closest concrete surface or two-thirds of the center-to-center spacing of bars being developed and shall not exceed 2.5d$_b$; k_1 is the bar location factor (1.3 when more than 300 mm of fresh concrete is placed below horizontal reinforcement, 1.0 for all other cases); k_2 is the concrete density factor (1.3 for structural low density concrete, 1.2 for structural semi-low-density concrete, 1.0 for normal-density concrete); k_3 is the bar size factor (0.8 for $A_b \leq 300$ mm^2, 1.0 for $A_b > 300$ mm^2); A_b is the area of an individual bar; k_4 is the bar fiber factor (1.0 for CFRP and GFRP, 1.25 for AFRP); and k_5 is a factor to consider bar surface (1.0 for surface roughened, sand-coated or braided surfaces, 1.05 for spiral pattern surfaces or ribbed surfaces, 1.8 for indented surfaces). It should be noted that according to CSA S806–12, the value of $\sqrt{f'_c}$ in Eq. (5) should not exceed 5 MPa. The results are present in column 8 of Table 5.

Furthermore, the Canadian Highway Bridge Design Code, CSA S6–19 [40], recommends chapter 16.8.4.1 to compute the development length for FRP bars in tension. Similarly, like CSA S806–12, there is no direct expression to compute the average bond strength. Consequently, Eq. (6) is provided to estimate the average bond strength of FRP bars to concrete after equating CSA S6–19 equation to Eq. (3). Where f_{cr} is the concrete cracking strength ($0.45\sqrt{f'_c}$) in MPa; K_{tr} is the transverse reinforcement index, representing the contribution of confining reinforcement; E_{frp} and E_s denote the elastic modulus of FRP and steel bar in GPa, respectively; f_y is the yield strength of transverse reinforcement in MPa; s is maximum center-to-center spacing of transverse reinforcement within the embedment length; n is the number of bars being developed along the potential plane of splitting; k_1 is the bar location factor (1.3 when more

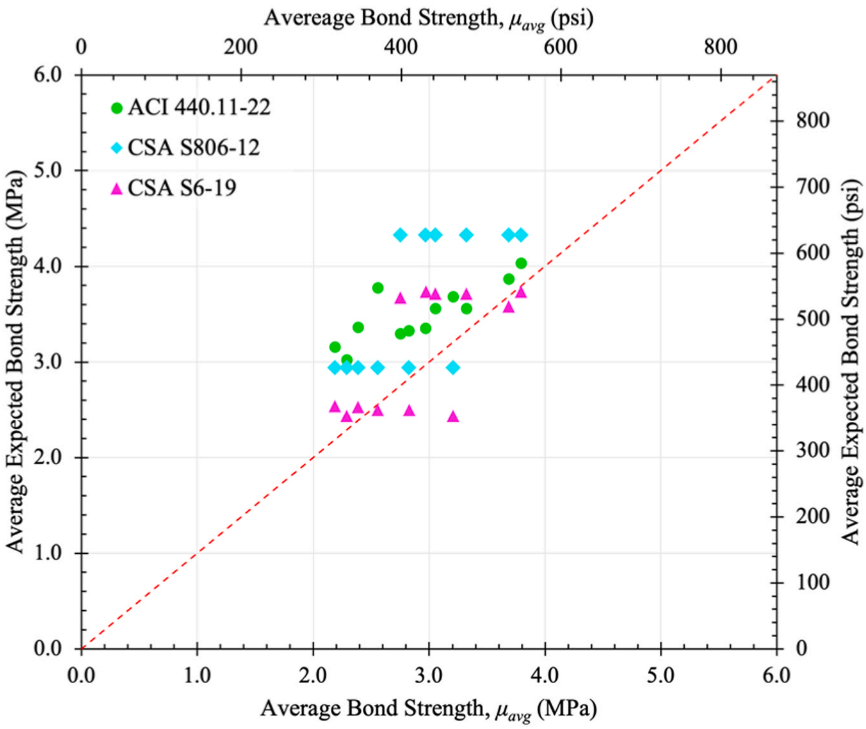

Fig. 15. Relation between the average bond strength from test and the average expected bond strength from codes/guidelines.

than 300 mm of fresh concrete is placed below horizontal reinforcement, 1.0 for all other cases); and k_4 is the bar surface factor, defined as the ratio of the bond strength of the FRP bar to that of a steel deformed bar with the same cross-sectional area as the FRP bar but not exceeding 1.0. In the absence of experimental data, k_4 shall be taken as 0.8. It should be noted that in the previous version (CSA S6–12), this factor resided in the denominator. This change led to a 64% decrease in bond strength values compared to the previous provision.

$$\mu_{S6-19} = \frac{f_{cr}(d_{cs} + K_{tr} \quad E_{frp}/E_s)k_4}{0.45\pi d_b k_1} \quad where \quad K_{tr} = \frac{A_{tr} f_y}{10.5sn} \tag{6}$$

Fig. 15 presents the relationship between the average bond strength observed in tests and the average expected bond strength as specified by codes/guidelines. The average predicted bond strength exceeded μ_{avg} by 17%, 19% and 39% for ACI 440.11–22, CSA S806–12 and CSA S6–19, respectively, indicating a lack of reliability in the predictions. The distant points on the CSA expression are for the 38 mm-cc specimens, which were more influenced by the concrete cover. d_{cs} is typically limited to $2.5d_b$; without this constraint, the predicted bond strength would have been even higher. Similarly, the restriction to $\sqrt{f'_c}$ in CSA S806–12 greatly limits the bond strength prediction. The influence of concrete cover in the CSA expressions is more pronounced than in the ACI expression. This restriction reduces the average bond strength by 21% compared to the value obtained without it. However, as depicted in Fig. 15, the values still exceed the test value. This implies that without this restriction, the CSA S806 provision would have been even more unconservative. A study by Gouda et al. [24] recommended increasing the limit of the square root of the concrete compressive strength to 8 MPa based on a conservative limit for beams that failed by splitting and pullout of GFRP bars.

Both, CSA expressions seem to have a more constant expected value without increments due to changes in length. ACI expression predicted values closer to observed results, primarily because the concrete cover in ACI is affected by the bar diameter and it just impact one component of the expression directly. Nevertheless, all expressions consistently overpredict the bond capacity of the beams. It is important to remember that these equations were developed for embedment lengths.

5. Conclusions

Four un-spliced and twelve lap-spliced GFRP-reinforced concrete beams were subjected to a four-point bending test. The GFRP specimens were reinforced with a single M16 (No.5) GFRP sand-coated rebar, designed to fail due to GFRP rupture (under-reinforced beam). The parameters under evaluation included the lap splice length, comprising three different configurations (i.e., 40-, 60- and 80-d_b), and the bottom clear concrete cover, involving two configurations (i.e., 19 mm and 38 mm). The presented study aimed to assess the accuracy of the current development length equation in predicting the bond strength of lap-spliced beams. Based on the results of this research study, the following conclusions can be drawn:

1. The experimental results revealed that the behavior of GFRP-RC beams was strongly influenced by the lap splice length and concrete cover. Inadequate lap splice lengths led to premature failure modes characterized by concrete splitting. The extensive, uniform flexural cracks observed in un-spliced specimens contrasted with the appearance of non-uniform cracks in lap-spliced beams. This highlights the importance of adequate lap splice lengths for effective stress transfer, which is critical in managing flexural cracks and preventing splitting-induced bond failure, ensuring structural integrity.
2. Lap-spliced and un-spliced specimens exhibited similar deflection levels under the same applied load. These findings suggested that excessive deflection may not be an early indicator of bond failure in GFRP-RC beams. Rebar slippage in lap-spliced specimens had a limited impact on bond stress transfer capacity and member flexural stiffness until reaching maximum slippage. Longer lap splice lengths allowed for greater rebar movement before experiencing brittle failure. Furthermore, strain gauges on the rebar showed non-linear stress distribution along the splice, primarily due to the initiation of beam cracking, emphasizing the complexity of bond behavior in GFRP-RC beams and its sensitivity to various parameters.
3. Concrete cover significantly influenced the behavior of lap-spliced GFRP-RC beams. Despite un-spliced specimens with 19 mm-cc having a theoretically higher ultimate moment, the smaller concrete cover in lap-spliced specimens made them more susceptible to splitting cracks, resulting in lower load-bearing capacity compared to 38 mm-cc specimens, which exhibited an average 21% higher capacity before failure. An analysis of the relationship between lap splice length and moment capacity revealed a linear increment of 0.39 kN·m per cm (0.73 kip·ft per in.) in moment capacity with increasing lap splice length. Reaching 100% capacity would have required longer lap splice lengths than those recommended by ACI 440.11–22 provisions. However, accounting for all strength factors, lap splice lengths of $119d_b$ (1.9 m) and $95d_b$ (1.5 m) were estimated for 19 mm-cc and 38 mm-cc specimens, respectively, representing reductions of 15% and 27% from ACI provisions.
4. The average bond strength between GFRP rebar and concrete was influenced by lap splice length, exhibiting a 7% increase for every $10d_b$ increment in lap splice length, with a significant 26% difference between 38 mm-cc and 19 mm-cc specimens. Bond stress distribution did not follow a linear pattern, likely due to non-uniform distribution of bond stresses and the influence of flexural crack initiation and propagation along the lap splice length. To prevent the introduction of a 'bond breaker' during strain gauge installation on GFRP rebar, one solution is to assume that rebar stress can be determined through a moment-curvature analysis independently of bond failure mode, allowing for the utilization of the full lap splice length for bond stress transfer, and thus avoiding the installation of strain gauges to measure rebar stress.
5. A comparison with the current ACI 440.11–22 code and alternative expressions from Canadian guidelines revealed significant variations in bond strength predictions. For 19 mm-cc specimens, the ACI expression overpredicted bond strength by an average of 24%, while for 38 mm-cc specimens, it overpredicted by 10%. Both Canadian guidelines (CSA S806–12 and CSA S6–19) showed overpredictions, averaging 19% and 4% higher bond strength, respectively. These discrepancies suggest that current equations may not reliably predict bond capacity for lap-spliced GFRP rebars. Variations in concrete cover significantly affected the bond predictions. Although CSA S6–19 presented a smaller overprediction, the values seemed not to be affected by the lap-splice length as found in the test results, and the 4% could be misinterpreted. The study highlights significant deviations when comparing the required lap splice lengths for full rebar capacity to ACI 440.11–22 provisions, indicating a need for revisions to ensure more accurate rebar capacity considerations in different scenarios, such as embedment length or lap splice length.

CRediT authorship contribution statement

Ortiz Jesus David: Conceptualization, Data curation, Formal analysis, Investigation, Methodology, Visualization and Writing - original draft. **Hosseini Seyed-Arman:** Writing – review & editing, Supervision, Resources, Project administration. **Hussain Zahid:** Writing – review & editing, Methodology, Investigation, Conceptualization. **Benmokrane Brahim:** Writing – review & editing, Supervision, Resources, Project administration, Funding acquisition. **Nanni Antonio:** Writing – review & editing, Validation, Supervision, Methodology, Funding acquisition, Conceptualization.

Declaration of Competing Interest

The authors declare that they have no known competing financial interests or personal relationships that could have appeared to influence the work reported in this paper.

Data Availability

Data will be made available on request.

Acknowledgments

Authors gratefully acknowledge the members of the Integrated Research Laboratory for the Development of Materials and Sustainable and Innovative Structures at the University of Sherbrooke in Canada, particularly Jérôme, Steven and Pascal for their invaluable support and assistance throughout the fabrication and testing process. Furthermore, to the Department of Civil and Architectural Engineering at the University of Miami for their significant contribution to this study. The authors gratefully acknowledge the financial support from the National Science Foundation IU-CRC Center for Integration of Composites into Infrastructure (CICI) under grant #1916342.

References

[1] M. Classen, J. Hegger, J. Bielak, J. Sch, Shear capacity of continuous concrete slabs with CFRP reinforcement, 320 (2022). https://doi.org/10.1016/j.conbuildmat.2021.126117.

[2] M. Ekenel, F.D.C. y Basalo, A. Nanni, Fiber-reinforced polymer reinforcement for concrete members, Concr. Int. 43 (2021) 18–22.

[3] A. Nanni, A. De Luca, H. Jawaheri Zadeh, Reinforced Concrete with FRP Bars: Mechanics and Design, CRC Press, 2014, https://doi.org/10.1201/b16669.

[4] A.V. Salan, M.K. Rahman, S. Al-ghamdi, J. Sakr, M.M. Al-zahrani, A. Nanni, A Monumental Flood Mitigation Channel in Saudi Arabia, Concrete International (2021) 33–41.

[5] J.D. Ortiz, S.S. Khedmatgozar Dolati, P. Malla, A. Nanni, A. Mehrabi, FRP-reinforced/strengthened concrete: state-of-the-art review on durability and mechanical effects, Materials 16 (2023), https://doi.org/10.3390/ma16051990.

[6] F. Yan, Z. Lin, M. Yang, Bond mechanism and bond strength of GFRP bars to concrete: a review, Compos B Eng. 98 (2016) 56–69, https://doi.org/10.1016/j.compositesb.2016.04.068.

[7] ACI Committee 440, Code Requirements for Structural Concrete Reinforced with Glass FRP Bars (ACI 440.11-22), American Concrete Institute, Farmington Hills, MI., 2022.

[8] ASTM Committee D30, D8505-23, Standard Specification for Basalt and Glass Fiber Reinforced Polymer (FRP) Bars for Concrete Reinforcement, ASTM International, West Conshohocken, PA. USA, 2023. https://doi.org/10.1520/D8505-23.

[9] Z. Hussain, A. Nanni, Design and detailing of glass fiber-reinforced polymer-reinforced concrete beams according to ACI 440.11-22, Acids Struct. J. (2023), https://doi.org/10.14359/51738744.

[10] H. Abbas, H. Elsanadedy, L. Alaoud, T. Almusallam, Y. Al-Salloum, Effect of confining stirrups and bar gap in improving bond behavior of glass fiber reinforced polymer (GFRP) bar lap splices in RC beams, Constr. Build. Mater. 365 (2023), https://doi.org/10.1016/j.conbuildmat.2022.129943.

[11] S.A. Hosseini, A.S. Farghaly, A. Eslami, A. Nanni, B. Benmokrane, Bond behaviour of lap spliced GFRP bars in concrete members: a state-of-the-art review and design recommendations, Constr. Build. Mater. 411 (2024), https://doi.org/10.1016/j.conbuildmat.2023.134714.

[12] B.W. Wambeke, C.K. Shield, Development length of glass fiber-reinforced polymer bars in concrete, Acids Struct. J. 103 (2006) 11–17.

[13] ACI Committee 318, Building Code Requirements for Structural Concrete and Commentary (ACI 318-19), American Concrete Institute, Farmington Hills, MI., 2019. https://doi.org/10.14359/51716937.

[14] C.O. Orangun, J.O. Jirsa, J.E. Breen, A reevaluation of test data on development length and splices, Acids J. Proc. 74 (1977) 114–122, https://doi.org/10.14359/10993.

[15] E. Makhmalbaf, A GFRP Bar Bond Stress and Strength: Comparison of Beam-bond and Pullout Tests Results, Master's thesis, McMaster University, 2015. http://hdl.handle.net/11375/17237 (accessed July 17, 2023).

[16] E. Makhmalbaf, A.G. Razaqpur, Development length of glass fibre reinforced polymer (GFRP) rebar based on non-uniform bond stress, Can. J. Civ. Eng. 49 (2021) 420–431, https://doi.org/10.1139/cjce-2020-0400.

[17] B. Basaran, I. Kalkan, E. Bergil, E. Erdal, Estimation of the FRP-concrete bond strength with code formulations and machine learning algorithms, Compos Struct. 268 (2021) 113972, https://doi.org/10.1016/j.compstruct.2021.113972.

[18] N. Saleh, A. Ashour, D. Lam, T. Sheehan, Experimental investigation of bond behaviour of two common GFRP bar types in high – Strength concrete, Constr. Build. Mater. 201 (2019) 610–622, https://doi.org/10.1016/j.conbuildmat.2018.12.175.

[19] ACI Committee 408, Bond and Development of Straight Reinforcing Bars in Tension (ACI 408R-03) (Reapproved 2012), American Concrete Institute, Farmington Hills, MI., 2003.

[20] B. Basaran, I. Kalkan, Development length and bond strength equations for FRP bars embedded in concrete, Compos Struct. 251 (2020), https://doi.org/10.1016/j.compstruct.2020.112662.

[21] N. Zemour, A. Asadian, E.A. Ahmed, K.H. Khayat, B. Benmokrane, Experimental study on the bond behavior of GFRP bars in normal and self-consolidating concrete, Constr. Build. Mater. 189 (2018) 869–881, https://doi.org/10.1016/j.conbuildmat.2018.09.045.

[22] A. Rolland, M. Quiertant, A. Khadour, S. Chataigner, K. Benzarti, P. Argoul, Experimental investigations on the bond behavior between concrete and FRP reinforcing bars, Constr. Build. Mater. 173 (2018) 136–148, https://doi.org/10.1016/j.conbuildmat.2018.03.169.

[23] A.C. Pay, E. Canbay, R.J. Frosch, Bond strength of spliced fiber-reinforced polymer reinforcement, Acids Struct. J. 111 (2014) 257–266, https://doi.org/10.14359/51686519.

[24] O. Gouda, A. Hassanein, K. Galal, Proposed development length equations for GFRP bars in flexural reinforced concrete members, J. Compos. Constr. 27 (2023), https://doi.org/10.1061/(asce)cc.1943-5614.0001272.

[25] A. Ruiz Emparanza, F. De Caso, A. Nanni, SP-356: Development length of GFRP rebars in reinforced concrete members under flexure, in: SP-356: Development Length of GFRP Rebars in Reinforced Concrete Members under Flexure, ACI Symposium Publication, 2022.

[26] S. Solyom, G.L. Balázs, Bond of FRP bars with different surface characteristics, Constr. Build. Mater. 264 (2020) 119839, https://doi.org/10.1016/j.conbuildmat.2020.119839.

[27] Y. Al-Salloum, L. Alaoud, H. Elsanadedy, A. Albidah, T. Almusallam, H. Abbas, Bond Performance of GFRP bar-splicing in reinforced concrete beams, J. Compos. Constr. 26 (2022), https://doi.org/10.1061/(asce)cc.1943-5614.0001190.

[28] Y. Man, T. Wang, Z. Wang, D. Wang, Study on the bond performance of glass fiber-reinforced polymer bars considering the relative position between longitudinal bars and stirrups, J. Build. Eng. 71 (2023), https://doi.org/10.1016/j.jobe.2023.106478.

[29] CSA, Design and Construction of Building Structures with Fibre-Reinforced Polymers (CSA S806-12 (R2017)), Canadian Standards Association, Mississauga, ON., Canada, 2012.

[30] C.P. Mosley, A.K. Tureyen, R.J. Frosch, Bond strength of nonmetallic reinforcing bars, Acids Struct. J. 105 (2008) 634–642, https://doi.org/10.14359/19947.

[31] N. Newman, A. Ayoub, A. Belarbi, Development length of straight FRP composite bars embedded in concrete, J. Reinf. Plast. Compos. 29 (2010) 571–589, https://doi.org/10.1177/0731684408100262.

[32] D.U. Choi, S.C. Chun, S.S. Ha, Bond strength of glass fibre-reinforced polymer bars in unconfined concrete, Eng. Struct. 34 (2012) 303–313, https://doi.org/10.1016/j.engstruct.2011.08.033.

[33] Y.C. Choi, K.H. Cho, B.Il Bae, H.K. Choi, Experimental study on the performance of tensile lap-spliced GFRP rebars in concrete beam, Mag. Concr. Res. 66 (2014) 1250–1262, https://doi.org/10.1680/macr.14.00111.

[34] C. Wu, H.J. Hwang, G. Ma, Effect of stirrups on the bond behavior of lap spliced GFRP bars in concrete beams, Eng. Struct. 266 (2022), https://doi.org/10.1016/j.engstruct.2022.114552.

[35] ASTM Committee C09, C39/C39M-21, Standard Test Method for Compressive Strength of Cylindrical Concrete Specimens, ASTM International, West Conshohocken, PA. USA, 2021. https://doi.org/10.1520/C0039_C0039M-21.

[36] ASTM Committee D30, D7913/D7913M-20, Standard Test Method for Bond Strength of Fiber-Reinforced Polymer Matrix Composite Bars to Concrete by Pullout Testing, ASTM International, West Conshohocken, PA. USA, 2020https://doi.org/10.1520/D7913_D7913M–14R20..

[37] ASTM Committee A01, A706/A706M-22a, Standard Specification for Deformed and Plain Low-Alloy Steel Bars for Concrete Reinforcement, ASTM International, West Conshohocken, PA. USA, 2022 10.1520/A0706_A0706M–22A.

[38] R. Aly, B. Benmokrane, U. Ebead, Tensile lap splicing of bundled CFRP reinforcing bars in concrete, J. Compos. Constr. 10 (2006) 287–294, https://doi.org/10.1061/ASCE1090-0268200610:4287.

[39] B. Tighiouart, B. Benmokrane, P. Mukhopadhyaya, Bond strength of glass FRP rebar splices in beams under static loading, Constr. Build. Mater. 13 (1999) 383–392, https://doi.org/10.1016/S0950-0618(99)00037-9.

[40] CSA, Canadian Highway Bridge Design Code (CSA S6:19), Canadian Standards Association, Mississauga, ON., Canada, 2019.